Bulk Photodriven CO2 Conversion through TiO2@Si(HIPE) Monolithic Macrocellular Foams

Bulk Photo-Driven CO_2 Conversion through TiO_2@Si(HIPE) Monolithic Macrocellular Foams

Sophie Bernadet[1,2], Eugénie Tavernier[2], Duc-Minh Ta[1], Renaud A. L. Vallée[1], Serge Ravaine[1,*], Antoine Fécant[2,*] and Rénal Backov[1,3,*]

[1] CRPP-UMR CNRS 5031, Université de Bordeaux, 115 Avenue Albert Schweitzer, 33600 Pessac, France.

[2] IFP énergies nouvelles - Lyon, Direction Catalyse et Séparation, BP-3, 69360 Solaize, France.

[3] Massachusetts Institute of Technology, Department of Civil and Environmental Engineering, 77 Mass. Av., Cambridge MA 02139, USA.

*Correspondence to: ravaine@crpp-bordeaux.cnrs.fr; antoine.fecant@ifpen.fr; backov@crpp-bordeaux.cnrs.fr; backov@mit.edu

ABSTRACT

Operating photo-induced reactions exclusively on catalyst surfaces while not exploiting the full catalyst volume generates a major foot-print penalty for the photo-catalytic reactor and leads to an inefficient use of the catalytic material. Photonic investigations clearly show that the solid foams are bearing a strongly multi-diffusive character, with photons being significantly trapped within the sample cores while addressing a photon mean free path $l_t = 20.1 \pm 1.3\ \mu m$. This 3D process greatly both limits back-reactions and promotes outstanding selectivity toward methane (around 80%) generation, and even ethane (around 18%) through C-C coupling reaction, with residual carbon monoxide and dihydrogen contents (around 2%). Silica-titania TiO_2@Si(HIPE) self-standing macrocellular catalysts lead to optimal efficient thicknesses up to 20 times those of powders, thereby enhancing the way for real 3D-photodriven catalytic processes above the millimeter scale and up to a 6 millimeters thickness. A rather simple Langmuir-Hinshelwood-based-kinetic-model is proposed which highlights the strong dependence of photocatalytic reaction rates on light

This is the author manuscript accepted for publication and has undergone full peer review but has not been through the copyediting, typesetting, pagination and proofreading process, which may lead to differences between this version and the Version of Record. Please cite this article as doi: 10.1002/adfm.201807767.

scattering and the crucial role on oxidation back-reactions. Besides, a strong correlation between light attenuation coefficient and photon mean free path and median pore aperture diameter is demonstrated, offering thus a tool for photocatalytic behavior prediction.

1. Introduction

Our modern society is facing the consequences of the earth's global warming, caused by the already critical levels of atmospheric carbon dioxide (CO_2), and aggravated by a continuous growing of the energy demand.[1-3] Since solar power could be considered at our timescale as an infinite energy source, solar-driven-fuel-production from CO_2 reduction is appearing at first glance as a smart and convenient alternative able to tackle the aforementioned issues simultaneously. The first main drawback is the intrinsic stability of CO_2. The C=O bond requires a dissociative energy of around 750 kJ mol^{-1} almost two times higher than the saturated C-H and C-C bonds, which have dissociation energies of around 430 kJ mol^{-1} and 336 kJ mol^{-1} respectively.[4,5] The thermodynamics implies that reaching the desired free enthalpy to generate saturated alkanes from CO_2 photoconversion is a daunting task, especially at room temperature. Other main drawbacks arise also from the photocatalytic process itself, i.e. light trapping and harvesting, charge separation-recombination and transportation, surface and backward reactions, which all need to be optimized. Additionally, since water in involved, the hydrogen evolution reaction (HER) enters into competition with CO_2 reduction and needs to be minimized. Actual strategies to solve these challenges are the subject of intense and highly competitive research. As the process is dealing with solar light interaction, either promising low bandgap materials such as carbon nitride or active species derivatives from high bandgap TiO_2 semi-conductor (by dye sensitization, doping, ...) are employed, addressing heterojunctions generation, noble metals adding, surface capping, atoms vacancies and so forth to optimize photocatalytic efficiency.[6,7] The main challenge of

optimizing solar irradiation concerns the two-dimensional character of the active layer. This is an issue for the efficiency in the whole set of artificial photo-driven processes beyond CO_2 photo-reduction, as for instance photo-catalyzed air or water treatment, photovoltaic, photo-induced water splitting, photo-fuel cells and so forth. Whatever the ingenious chemistry deployed at the molecular level, common sense is pleading to increase the surface/volume ratio of the photo-active materials in use, giving thereby rise to a severe foot-print penalty. Although recent studies have shown that light trapping within an active layer is a critical criterion for improving the efficiency of optoelectronic devices such as thin solar cells, photoelectrochemical cells and photo-fuel cells,[8-15] all these photonic investigations and photo-conversion improvements are still dealing with thin films which exhibit a surface behavior rather than a bulk one.

2. Results and discussion

Solid foams bearing a hierarchically organized porosity are perfect candidates to achieve three-dimensional CO_2 photoconversion.[16,17] One synthetic path to reach those hierarchical architectures is making the use of a synergistic template effects while combining lyotrope mesophases (concentrated micelles) which create the mesoporosity (pore diameters ranging from 2 nm to 50 nm) and concentrated oil-in-water emulsions inducing the connected macroporosity (pore diameters above 50 nm), combined with the sol-gel process that condenses the continuous hydrophilic phase.[18] As the inorganic skeleton is amorphous silica, the microporosity (pore diameters below 2 nm) relies on the statistical repartition of SiO_4 tetrahedra within the geometric space. These self-standing foams are labelled Si(HIPE),[19] H.I.P.E. being the acronym for High Internal Phase Emulsion[20] and they can be hybridized for other heterogeneous catalysis applications.[19,21] When being purely inorganic, these foams

have been recently employed as light scavengers in the field of random lasing[22,23] where TiO_2 has been added during the sol-gel process to increase the inorganic skeleton refractive index, thereby optimizing the photon mean-free-path within the foams.[24]

2.1 Material syntheses and characterizations

The synthetic route employed in this study was, in a first step, the generation of Si(HIPE), that acted as a host for the heterogeneous nucleation of TiO_2 nanoparticles performed in a second step (*see experimental section*). We labeled these foams TiO_2@Si(HIPE). After being sintered at 400°C for 1 hour, the resulting materials are monolithic self-standing foams **Figure 1a**.

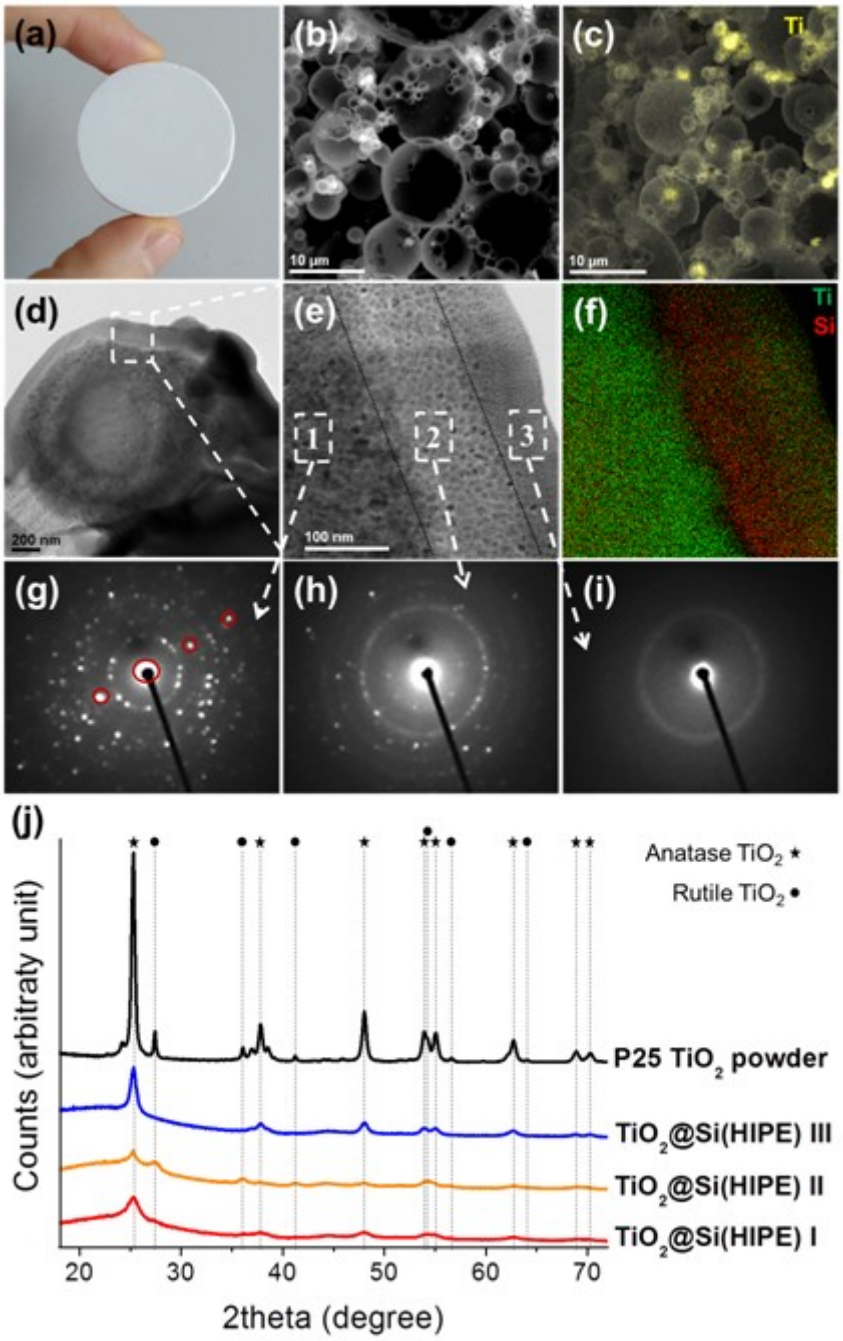

Figure 1. Multi-scale characterizations of TiO_2@Si(HIPE) monoliths and crystalline structure of commercial reference TiO_2 (P25 TiO_2 Degussa). (**a**) Photograph of a typical TiO_2@Si(HIPE). (**b**) SEM image of a typical TiO_2@Si(HIPE), at 15 kV, where TiO_2 particles appear brighter. (**c**) SEM-EDS mapping of a typical TiO_2@Si(HIPE) where titanium element is highlighted in yellow. (**d**) HR-TEM image of TiO_2 typically embedded in a silica hollow sphere. (**e**) Higher magnification of (d) HR-TEM image showing three domains. (**f**) TEM-EDS mapping of (e) HR-TEM image, highlighting the distribution of titanium (in green) and silicon

(in red) elements. (**g, h** and **i**) Respectives SAED patterns of region 1, 2, and 3 of (**e**): (**g**) poly-nanocrystalline area with a large number of crystals, with the appearance of a reticular plane, (**h**) poly-nanocrystalline area with a few crystals, (**i**) amorphous area. (**j**) XRD patterns of the tested photocatalytic materials; depicting a mixture of anatase (★) and rutile (●) crystalline phases for TiO_2@Si(HIPE) II and P25 TiO_2, whereas monoliths TiO_2@Si(HIPE) I and III provide only the anatase crystalline phase.

These monoliths are bearing open macroporosity (Figure. 1b) and TiO_2 nanoparticles homogeneously dispersed within the whole foam (Figures. 1, c and 1f). TiO_2 is heterogeneously nucleated directly at the surface of the silica walls (Figures. 1e and 1f). This is a rare feature as during the liquid-phase hydrolysis in the excess of water, water molecules formed a thin film on the modified matrix surface and easily cleaved the Si-O-Ti bonds to afford discretized SiO_2 and TiO_2 phases.[25] In the present synthetic path, we do not observe such phase segregation.

When considering the Figures 1e and 1i the first layer of TiO_2 present in the vicinity of the silica walls remains amorphous even after the thermal treatment. The TiO_2 crystallinity increases when moving away from the silica-titania interface (Figures. 1g and 1h). The amorphous silica network is blocking the crystallization of the titania network at the SiO_2-TiO_2 interface. As such, when using fresh titanium alcoholate precursor (TiO_2@Si(HIPE)s I & III), the nucleation events at the silica surface are favored and crystal growth minimized. As such, the titania transition from amorphous to crystalline allotropic form is stopped at the anatase state and the rutile form is never reached, contrary to what is observed with pure titania meso-macrocellular foams.[26,27] Aging the titanium alcoholate precursor (TiO_2@Si(HIPE) II), on the contrary allows the homogeneous nucleation of TiO_2 nuclei in solution in addition to the monomolecular entity.[28] If the molecular alcoholate might proceed the same way as TiO_2@Si(HIPE)s I & III, pre-condensation within the starting sol

would increase the nuclei-nuclei interface during impregnation step leading to a anatase-rutile allotrope transition at much lower temperature.[29] This pseudo epitaxial phenomenon demonstrates that in the present case, at the molecular level, the Si-O-Ti bonds at the silica/titania interfaces are not cleaved, as the amorphous silica network can hinder the TiO_2 crystallization upon thermal treatment, when no pre-hydrolyzed sols are employed. At the macro- and mesoscopic length scales, the TiO_2@Si(HIPE) pore volumes are around 75 %, their skeleton and apparent densities are ranging respectively from 0.4-0.55 g cm^{-3} and 0.11-0.13 g cm^{-3} while offering specific surface areas between 250-460 m^2 g^{-1} emerging essentially from the amorphous silica microporosity (*see experimental section and figures S1-S3*).[30]

2.2 Photonic investigations

In order to characterize the optical diffusion properties of the various samples, we recorded the times of flight of individual photons travelling across the sample relative to the incident pulse, owing to a simultaneous spatial and time-resolved setup. **Figure 2** shows the recorded two-dimensional streak plots for the L = 8.5 mm thick TiO_2@Si(HIPE) I (a) and a L = 2.0 mm thick TiO_2 powder (b). Considering Figure 2, the samples clearly exhibit a strongly multi-diffusive character, with photons being significantly delayed in the sample in both cases. The packing of the grains in the TiO_2 powder results in a mean exit time of light longer than in TiO_2@Si(HIPE) I. A small crack is evidenced in the latter, causing a part of the excitation pulse to exit early, as observed by the line at about 0.8 ns. In order to quantitatively characterize the samples and obtain the light diffusion parameters as the transport mean free path l_t and the inelastic absorption length l_i, we firstly extracted the temporal profiles of light transmitted by the samples in the forwards direction, as shown by the horizontal lines drawn

in the streak plots (Figures. 2a and 2b). We then fitted them with the full solution of the diffusion equation (*see section 3 in SI*), valid for $\lambda \ll l_t \ll L$ at all times for a δ-function light source.[31,32]

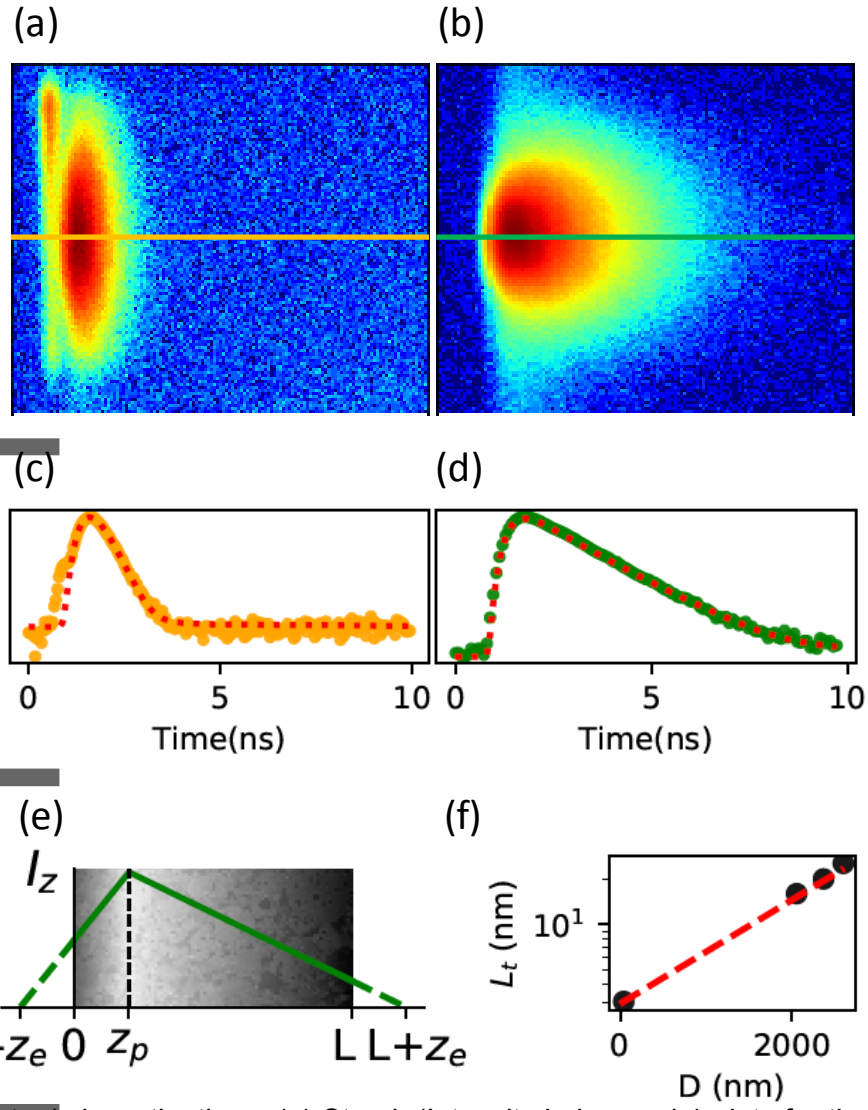

Figure 2. Photonic investigations. (**a**) Streak (Intensity in log scale) plots for the L = 8.5 mm thick TiO_2@Si(HIPE) I and (**b**) for a L = 2.0 mm thick TiO_2 powder (horizontal axis: spatial diffusion, vertical axis: time delay). (**c** and **d**) Respective (semi log) temporal decay profiles extracted at the maximum intensities (orange and green horizontal lines in (a) and (b), respectively) and fitted by the full solution of the diffusion equation (red dashed lines). (**e**) Energy distribution (green solid line) for a 1D diffusive system in the case of a delta-like source. The grey zone represents the region occupied by the sample and the green dashed lines show the linear extrapolations of the intensity out of the sample. (**f**) Transport mean

free path (l_t) values as compared to median pore aperture diameter (D) for the bed powder and TiO_2@Si(HIPE)s. The absolute errors on l_t range between 0.3 and 1.3 μm, i.e. so small that they lie within the size of the represented experimental dots. A strong exponential correlation between the two parameters is clearly observed (R^2 = 0.9995).

These profiles and their corresponding fits are shown on a semi-logarithmic plot in Figures. 2c and 2d. The full solution of the diffusion equation is outlined in section 3 in *SI* and exemplified in Figure 2e. The extrapolation length (z_e) is the position where the diffusive mode nulls. The penetration length (z_p) is the position of the effective source for the source equation. z_p thus also signals the position of maximum intensity in the sample. These two lengths are generally set identical and match $z_0 = \frac{2}{3} l_t \left(\frac{1+R}{1-R}\right)$ in the case of no absorption. The proper reflectivities R are set at the boundaries (*28*). Owing to this simple model of light diffusion through a slab geometry, the temporal profiles obtained experimentally could be appropriately fitted (Figures. 2c and 2d). The extracted values for the transport mean free paths are $l_t = 20.1 \pm 1.3\ \mu m$ and $l_t = 3.1 \pm 0.3\ \mu m$ for TiO_2@Si(HIPE) I and the TiO_2 powder, respectively. However, the inelastic absorption length proved to be a rather insensitive parameter of the fit, revealing a very weak absorption of the samples at the chosen excitation wavelength, as we already observed and reported in previous experiments on similar materials.[22-24] Based on these results, the light penetration length for which the maximum intensity will be observed in the samples is $z_p = z_0 \cong \frac{2l_t}{3}$. As such, the light penetration depths are expected to be slightly less than one order of magnitude larger in TiO_2@Si(HIPE) I with $z_p \cong 13\ \mu m$ to compare with $z_p \cong 2\ \mu m$ for the powdered sample (note that these results were obtained using of 300 fs pulses at a 515 nm wavelength excitation). The photocatalytic activity of TiO_2@Si(HIPE)s can thus be expected, on purely photonic basis, to occur more in the bulk of the system than what has been usually observed

for powders (even if the precise values of z_p just reported will not be strictly transferrable in the excitation conditions of the photocatalytic experiments). Furthermore, as illustrated in Figure 2f, a strong exponential correlation between transport mean free paths and mean pore aperture diameters of materials is observed, which correspond to the diameter of connecting windows between adjacent hollow spheres (*see section 1 in SI*). This leads to the conclusion that a reduction of the bouncing frequency induced by increasing the distance between cell walls is favorable to the enhancement of the photon transport mean free path. We can thus presume that light transport within these foams is strongly dependent on this diameter and can be tuned through the material's texture and porosity.

2.3 Photocatalytic process

To gather first visual evidences of photocatalytic bulk behavior of TiO_2@Si(HIPE)s, photoreduction of chloroauric salt impregnated within the whole porosity of such a monolith has been carried out. The photoreduction creates gold nanoparticles of purple color. **Figure 3** highlights that photons penetrate the entire material thickness of several millimeters when looking at the longitudinal section.

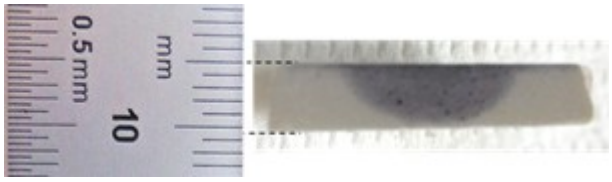

Figure 3. Gold photoreduction within TiO_2@Si(HIPE)s as a colored probe. A gold salt solution of 10^{-2} M was prepared from $KAuCl_4$ in 2-propanol solvent. TiO_2@Si(HIPE)s were then impregnated under vacuum in a desiccator. Chloroaurate ions were reduced during 1 hour into gold nanoparticles under UV irradiation provided by a metal halide lamp (240 W/m² - λ = 280-395 nm) located 5 mm above monolith surface by the mean of optical fiber waveguide.

Thus, artificial photosynthesis experiments (*see section 2 in SI*) have been performed with the set of various TiO_2@Si(HIPE)s as compared to what could be a classical implementation employing a TiO_2 nanopowder bed. **Figure 4a** shows a peculiar trend for TiO_2 powder activity because an optimum is found for about 360 µm bed thickness (or 0.11 kg m^{-2}) after which a continuous decrease is observed. It is more likely expected to observe a continuous increase of activity per geometric surface when increasing thickness (more active phase) until a plateau due to shadow effect.[33] We suggest this phenomenon is due to an increasing adsorbed oxygen concentration gradient within the catalytic bed favoring the back-oxidation reaction of the products (H_2, CO, CH_4) by O_2, until the photon concentration falls short leading to a plateau in activity.

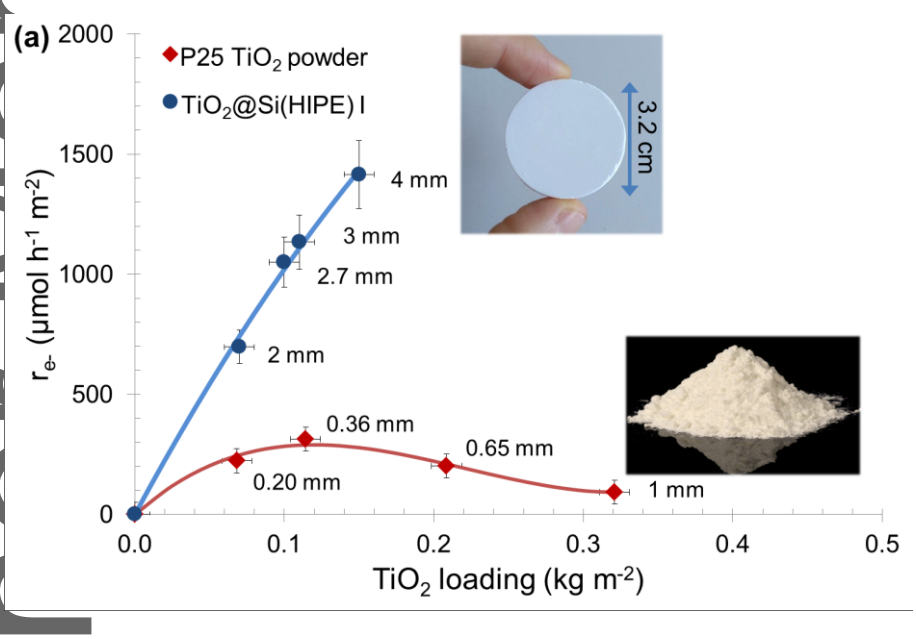

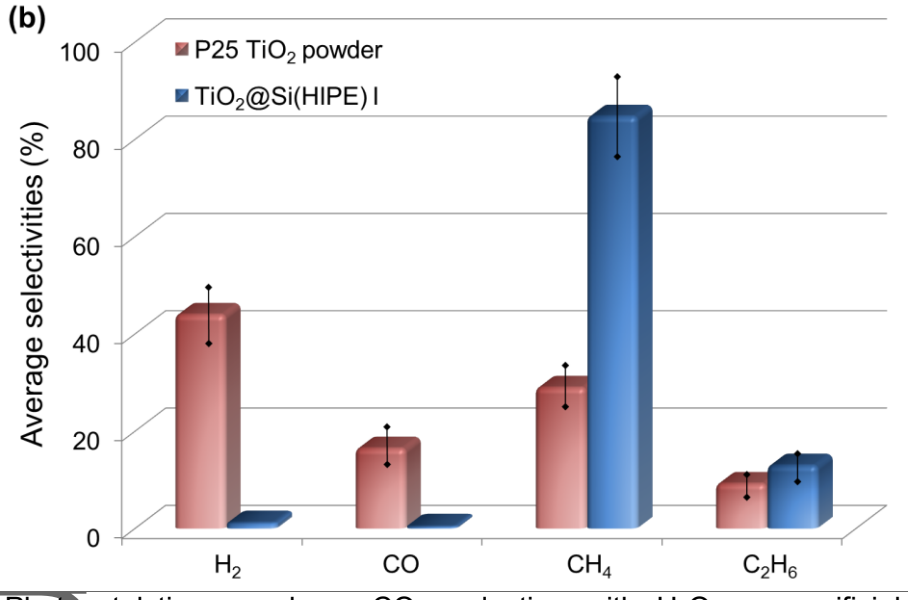

Figure 4. Photocatalytic gas phase CO_2 reduction with H_2O as sacrificial agent. (**a**) Photocatalytic activities of TiO_2@Si(HIPE) I and TiO_2 powder bed are represented by "r_{e^-}" the average electron consumption rate normalized by time and geometric surface as compared to TiO_2 loading per surface unit – as complementary information bed thickness values are labeled; solid lines show trends and no modelling at this point (**b**) Product selectivity is provided for dihydrogen, carbon monoxide, methane and ethane, which are the reduction products detected for both materials. Performances are given with a relative standard deviation of 10%.

With TiO_2@Si(HIPE) I, the behavior seems to be significantly shifted to a thicker photocatalytic bed as maximum activity is not reached even for a thickness more than ten times greater than that of the powder bed (> 4 mm). These results lead us to the conclusion that TiO_2@Si(HIPE) I allows enhanced photon penetration as already suggested by optical diffusion properties characterization, and furthermore greatly limits back-reactions. We are now facing a bulk photo-driven scenario rather than the commonly observed surface scenario, where a thicker bed actually works better (up to 4 mm). Beyond, Figure 4b also suggests that TiO_2@Si(HIPE) I favors multi-electronic reactions as CH_4 and C_2H_6 are main products (94%) and require 8 and 14 electrons respectively, whereas TiO_2 as powder is reaching a selectivity of 62 % for H_2+CO which require only two electrons. This enhanced selectivity

might be related with the fact that photons concentration is higher within the thickness of TiO_2@Si(HIPE) I, leading to enhanced electron density on the TiO_2 particles surface.

2.4 Kinetic investigation and modelling

Kinetic modeling has been carried out based on the Langmuir-Hinshelwood formalism for chemical reactants and considering all redox reactions in which observable reagents and products may be involved. The modeling was also intended to account for the photon concentration profile within the photocatalytic bed in the axial direction, and for this purpose we assumed that it follows a Beer-Lambert law. Those assumptions and full calculation of the rate equation are reported in details (see *section 3 of SI*). Thus, considering photon penetration within the material thickness, reduction reaction of CO_2 to CO, CH_4 and C_2H_6, co-reduction of H_2O to H_2, and inverse reaction of O_2 reduction to H_2O, we end up with the following activity equation as a function of the bed thickness h (*section 3 in SI*):

$$r_{e-}(h) = \frac{k_0 . E(h) . {C_s}^{irr}(h)}{S^{irr}} \times \frac{K}{(K + E(h)^4)} \quad \text{(Eq.1)}$$

With:

$$E(h) = E^0 \times \int_0^h e^{-\alpha . z} . dz \quad \text{(Eq.2)}$$

$${C_s}^{irr}(h) = C_s \times \int_0^h e^{-\alpha . z} . dz \quad \text{(Eq.3)}$$

$r_{e-}(h)$ being the rate of electron consumption for H_2, CO, CH_4 and C_2H_6 production in mol h^{-1} m^{-2}, k_0 being kinetic constant for electron-hole pairs generation, K being simplified apparent kinetic constant for redox reactions, $E(h)$ being molar quantity of absorbable photons (315-400 nm) within the bed thickness h, ${C_s}^{irr}(h)$ being molar quantity of irradiated TiO_2 surface sites within the bed thickness h, S^{irr} being the geometric irradiated section of

the material. Also, E^0 being the molar quantity of absorbable photons per unit of depth without attenuation, C_s being molar quantity of TiO_2 surface sites per unit of depth, α being an attenuation coefficient related to the Beer-Lambert law. As illustrated in **Figure 5**, activity plots as a function of bed thickness for TiO_2 powder bed and the set of prepared TiO_2@Si(HIPE)s I, II and III revealing diverse activities (partially related to crystallinities, TiO_2 loadings and particle sizes) were used to fit the model to experimental data. By adjusting k_0, K and α for each material we were able to fit the data with a very good agreement, highlighting the strong dependence of photocatalytic reaction rates on light scattering, supporting our previous hypotheses about deeper photon penetration within TiO_2@Si(HIPE)s, and the crucial role on oxidation back-reactions. k_0 value is found higher for TiO_2 P25, meaning that the well-known commercial powder is intrinsically more efficient to create reactive electron-hole pairs at TiO_2 surface slab by photon absorption than the in-situ generated TiO_2 phases during TiO_2@Si(HIPE) synthesis.

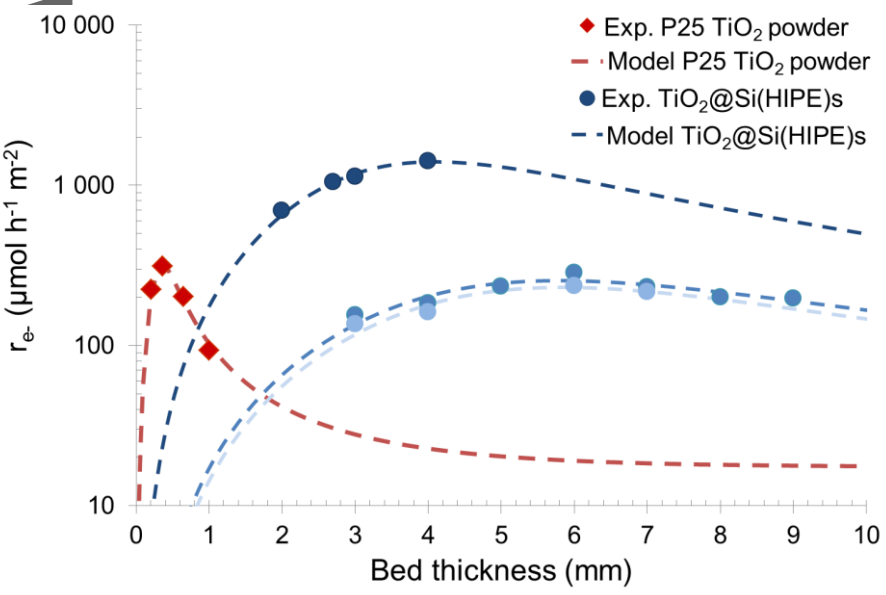

Figure 5. Modeling "r_e" (average electron consumption rate normalized by time and geometric surface) as compared to bed thickness for photocatalytic gas phase CO_2 reduction with H_2O as sacrificial agent. Experimental data are given as diamond for TiO_2 powder and circle with shades of blue, from the darkest to the lightest for TiO_2@Si(HIPE)s I, II and III, respectively. Dashed lines correspond to the best fits of kinetic modeling for each sample. Because of log scale on r_e axis, error bars lie within the size of the represented experimental dots given with a relative standard deviation of 10%.

Nevertheless, HIPE-based carriers allow better light penetration, α is significantly reduced, (*see Table S9 in SI*), i.e. a higher quantity of efficient photons compared to the whole bed volume (*see Fig. S9 in SI*). Hence, this better efficiency leads to constant activity per gram as the mass of photocatalyst is increased until deeper catalytic bed (meaning almost no light attenuation) when that of the powder decreases excessively rapidly (*see Fig. S10 in SI*). Moreover, a decrease of the reverse reaction by O_2 reduction and H_2 and/or C_xH_y oxidation for TiO_2@Si(HIPE)s is probably linked to the active phase dilution within the macroporous SiO_2 carrier leading to lower θ_{O2} onto the TiO_2 surface. Indeed, we observe a correlation between the constant K derived from the kinetic model with the relative contribution of specific surface area for TiO_2 nanoparticles (*see Fig. S11 in SI*). At higher K, the reverse reaction rate is assumed to be lower. Furthermore, a strong correlation between light attenuation coefficient α and photon mean free paths l_t or median pore aperture diameter (as both are linked, as showed in Fig. 2f) is made obvious in **Figures. 6a** and **6b**.

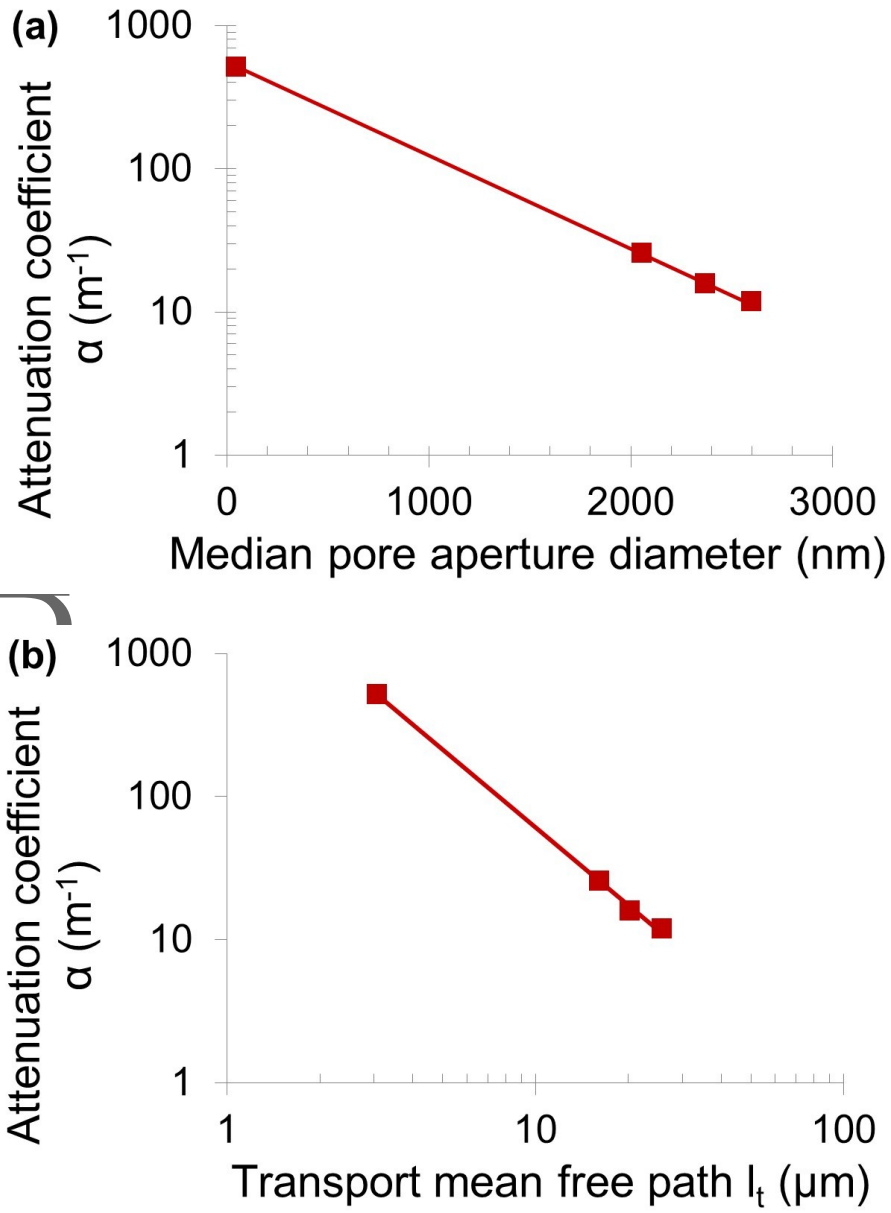

Fig. 6. Comparison between photonic and textural properties**.** Beer-Lambert attenuation coefficient α extracted from kinetic modeling reported as a function of (**a**) median pore aperture diameter given by Hg porosimetry for TiO_2@Si(HIPE)s and by geometric model for TiO_2 powder and (**b**) transport mean free paths l_t obtained from photonic characterization, with strong correlation: respectively R^2 = 0,9998 for (**a**) and R^2 = 0.9998 for (**b**). Hg porosimetry data are given with a relative standard deviation of 3%.

This means that photocatalyst performances are indeed highly predictable by knowing bed porosity and/or by measuring photon transport within. TiO_2@Si(HIPE)s act as

very efficient “photonic sponges” thanks to its internal architecture. This term was earlier suggested by Garcia *et al.*[34] for hard templated porous thin films of TiO_2 with much lower pore aperture, work which did not demonstrate any thickness advantages according to attenuation coefficient α dependence with pore size, as now revealed by this work

3. Conclusion

Preparation of novel silica-titania self-standing porous materials opens the path for real 3D-photodriven catalytic processes. The counter intuitive scenario of “thicker is better” becomes now a reality above the millimeter length scale with this set of materials with optimal efficient thicknesses up to 20 times those of powders. The first immediate benefice is the dramatic decrease of the foot-print penalty when addressing solar fuel production. Photonic investigations clearly show that the solid foams are bearing a strongly multi-diffusive character, with photons being significantly trapped within the sample cores while addressing a photon mean free path $l_t = 20.1 \pm 1.3\ \mu m$. This 3D process greatly both limits back-reactions and promotes outstanding selectivity toward methane (around 80%) generation and even ethane (around 18%) through C-C coupling reaction with residual carbon monoxide and dihydrogen contents (around 2%). In order to offer a better understanding of the light scattering-induced CO_2 reduction process a simple kinetic model has been carried out based on a Langmuir-Hinshelwood formalism while considering all redox reactions in which observable reagents and products may be involved. The outstanding agreement between the model and the experiments highlights the strong dependence of photocatalytic reaction rates with light scattering while underlying the crucial role on oxidation back-reactions. Also, a strong correlation between light attenuation coefficient and photon mean

free paths and median pore aperture diameter is demonstrated, offering thus a tool for photocatalytic behavior prediction. This aspect could find direct application while employing Pickering-based silica foams as hosts where both cell diameters and cell junctions can be tuned on demand and independently.[35] Moreover, this work raises two particularly important issues: first the strong photon supplying dependence observed here is weakening the widely assumed $CO_2^{\bullet-}$ radical formation as the rate limiting step for CO_2 photoreduction,[7] second it is also pointing out the need to not be satisfied with standardized results per unit of photocatalyst mass (usually µmol h^{-1} g^{-1}), but supplemented by unit of geometric irradiated area (µmol h^{-1} m^{-2}) since this will ultimately be the sizing factor of future systems (its foot-print). Beyond the host foam morphologies, photo-reactivity enhancement is to be expected on a chemistry viewpoint while transposing this study toward effective semiconductor acting within the visible light wavelength.[6,7] This work is opening a bright future not only for solar fuel production, but also for photo-induced air purification, water splitting systems and/or for photovoltaic devices where light trapping being effective toward photocatalysis at several millimeters length scale.

4. Experimental section

Materials: TiO2@Si(HIPE) synthesis needs the following products. The titanium dioxide and silica precursors, titanium(IV) isopropoxide (TTIP) and tetraethyl orthosilicate (TEOS), were purchased from Sigma-Aldrich (purity 97% and ≥ 99%, respectively). The surfactant, tetradecyltrimethylammonium bromide (TTAB), was also furnished by Sigma-Aldrich (purity ≥ 99%). The solvent isopropanol (2-propanol), and hydrochloric acid (HCl), were purchased from VWR Chemicals (purity ≥ 99% and 37% respectively). Then, the oily phase, dodecane was furnished by Alfa Aesar (purity 99%). Titanium dioxide (P25) powder was

purchased from Sigma-Aldrich (purity ≥ 99.5%). KAuCl4 powder was purchased from Sigma-Aldrich (purity = 99.995%). For photocatalytic tests, CO2 is purchase from Air Liquide (purity > 99%). Water used for material synthesis and poured in the water tank for photocatalytic tests is demineralized water with resistivity > 10 MΩ**.**

Syntheses: TiO_2@Si(HIPE) synthesis was a two steps route. The first step was the synthesis of silica-based self-standing foams, built on the use of both micelles and direct concentrated emulsion templates, and labelled Si(HIPE) (16), H.I.P.E. being the acronym for High Internal Phase Emulsion. Typically, 5 g of TEOS was added to 21.9 g of TTAB acid aqueous solution at 35% in weight (5 mL of HCl 37%). This biphasic TEOS/water solution was mixed until complete hydrolysis of TEOS, i.e. until a monophasic solution is obtained. Then, the oil emulsification process was carried out by adding 35 g of dodecane drop-by-drop in a mortar and manual stirring with a pestle. This final sol was then transposed in a Petri dish. Other plastic recipients can be used depending on the shape wanted. The whole was placed in a desiccator during one week, with a water bottom, in order to provide water molecules in continuous during the condensation process and prevent material cracks. The resulting material was then washed by immersion in THF during 24 hours to bulky remove dodecane, and finely in a (70:30) THF/acetone mixture during 3 days, renewed every day. Finally, wet gels were dried in desiccator during almost one month, before being thermally treated. This treatment aimed to remove the organic supramolecular-type templates, and sinter the material optimizing mechanical strength. The heating speed was monitored at 1°C min^{-1} with a first plateau for 2 hours at 120°C (removing chemisorbed water), a second at 180°C (removing structural water) and then at 650°C for 5 hours. The cooling process was uncontrolled and

directed by the oven inertia. The second step was the impregnation of titanium dioxide precursor or powder (P25).

TiO_2 precursor impregnation: The differences between the three monoliths presented are detailed below and summarized in Table S1. Hydrochloric acid aqueous solution (around 30% vol. of HCl) and isopropanol were mixed under magnetic stirring, (1:1) proportion. Then, TTIP was added to obtain a concentration of 0.29 M for TiO_2@Si(HIPE)s I & II, and 0.22 M for TiO_2@Si(HIPE) III of titanium dioxide precursor in the solution. After 2 hours of stirring, Si(HIPE)s were put in the solution. The whole was then placed in a desiccator, in which vacuum is done until 30 mbar, until effervescence stop, in order to extract air from Si(HIPE)s. Several vacuum cycles were done until Si(HIPE)s fell to the solution bottom (d_{SiO2} > dsolution), and even remained there under vacuum. Then, a static vacuum was done and hold during 16 hours. After this aging step, monoliths were removed from the solution, and placed between two sheets of absorbent paper, during two weeks. Once dry, a new impregnation step in the same conditions was operated (except for TiO_2@Si(HIPE) II for which the impregnation solution is 38h old). Finally, a thermal treatment had to be carried out in order to crystallize TiO_2 particles. The crystal structure depends on the loading rate of TiO_2 and the temperature applied. In this study case, the heating speed was monitored at 1°C min^{-1} with a first plateau for 2 hours at 120°C and then at 400°C for 5 hours. The cooling process was uncontrolled and directed by the oven inertia.

Material characterizations: TEM coupled with EDS experiments were performed with a JEOL JEM 2200FS microscope (accelerating voltage of 200 kV). The TiO2@Si(HIPE) sample was prepared by ion milling process using a Gatan 691 PIPS of a piece of monolith

deposited on a Nickel grid with holes. This preparation method allows the sample to be thinned while maintaining its structure. SEM observations were performed with a FEI Nova nano SEM 450 scanning electron microscope operating at 5 kV or 15 kV, to modulate the contrast between SiO_2 and TiO_2. Operating at low vacuum, no sample metallization is needed. X-Ray Diffraction (XRD) experiments were carried out on a PANanytical X'Pert PRO MPD diffractometer, with a copper X-ray source (λ(Cu Kα) = 1.5418 Å). The scattered radiation was collected on two detectors: a punctual detector and a X'Celerator rapid detector. Both are preceded by a secondary graphite crystal monochromator. Crystallite sizes were calculated from XRD patterns and Scherrer equation**:** X-Ray Fluorescence (XRF) semi-quantitative analyses were carried on PERFORM'X Sequential X-Ray Fluorescence Spectrometer, from Thermo Fisher Scientific. The wavelengths of X-rays emitted by the bombarded matter are characteristics of atoms. Then, Ti and Si element contents were measured and thus the TiO_2 mass percentage can be determined with an uncertainty of the order of 20%, due to the semi-quantitative method. Diffuse reflectance UV/Vis spectroscopy is routinely used to determine the bandgap energy of semiconductors (active phase). The Kubelka-Munk (KM) function is used to describe the diffuse reflection and to obtain the bandgap energy from the plots of [F(R)hν]1/2 in function of hν photons energy, as the intercept of the extrapolated linear part of the plot at [F(R)hν]1/2 = 0. Measurements were performed on Agilent CARY 60 UV-Visible spectrometer, and the reference (infinitely reflective compound) used is a Spectralon one. The pore size distributions obtained by mercury intrusion porosimetry of TiO_2@Si(HIPE)s I, II and III are shown in Figs. S1A, S2A and S3A, respectively. For all, the macroscopic cell window distributions were obtained. Actually, this technique only measures pore diameters that minimize mercury infiltration.

Thus, the pore size distributions correspond to the interconnections between pores, not to the pores themselves. These interconnections are called cell windows. The pore size distributions show a polydispersal distribution, which is explained by the structure of the material in aggregated hollow spheres. This polydisperse character is related to the window size distribution which spreads from around 10 up to 5000 nm, with a peak centred around 2 µm. This peak corresponds to the interstices formed at the junction of three (or more) hollow silica spheres; these are the so-called "external" windows. The shoulder at this peak corresponds to the "internal" windows formed by the junction between two walls of adjacent hollow spheres. Unlike TiO_2@Si(HIPE)s I and II, TiO_2@Si(HIPE) II has a higher mesoporosity share centred on around 30 nm. The bimodal character, associated with the two contributions respectively cantered at 30 nm and 2 µm (Fig. S3), is commonly observed for Si(HIPE)s structure. On one hand, impregnation with two fresh solutions favours the nucleation of TiO_2 in mesopores. On the other hand, the second impregnation of TiO_2@Si(HIPE) II (with an aged TIPP impregnation solution) leaves more mesopores free. Nitrogen isotherms of TiO_2@Si(HIPE)s I, II and III are shown in Figs. S1B, S2B and S3B, respectively. According to IUPAC nomenclature (30), they provide a type I – IV with a narrow H4 hysteresis, testifying to a highly microscopic and weakly mesoscopic porosity. Microporosity, intrinsic to the amorphous structure of silica, represents more than 80% of the porous volume probed by nitrogen. All characteristic values of TiO_2@Si(HIPE)s and TiO_2 P25 powder are summarized in Tables S2, S3 and S4. Materials specific surface areas and pore characteristics at the mesoscale were obtained with a Micromeritics ASAP 2420 employing the Brunauer-Emmett-Teller (BET) and Barrett-Joyner-Halenda (BJH) methods. Intrusion/extrusion mercury measurements were performed using a Micromeritics Autopore

IV apparatus to determine the pore size distribution, and especially, the median pore aperture diameter.

Supporting Information

Supporting Information is available from the Wiley Online Library or from the author.

Acknowledgments

We thank D. Uzio for his participation during the building of the project, V. Lameiras Franco Da Costa for kinetic discussions, and finally G.D. Pirngruber and A.T. Fialho Batista for their attentive reading of the manuscript.

Funding: This work was supported by IFPEN PhD funding contract number 419398/ CNRS 129590.

Conflict of Interest.

Authors declare patents filling FR 17/53.757 and FR 17/53.758 related to the project.

Keywords: Porous materials, CO_2 photo-reduction, heterogeneous catalysis, sol-gel process, integrative chemistry.

Received: ((will be filled in by the editorial staff))
Revised: ((will be filled in by the editorial staff))
Published online: ((will be filled in by the editorial staff))

References

1. D.G. Nocera, *Chem. Soc. Rev.* **2009**, *38*, 13.
2. N.S. Diffenbaugh, D. Singh, J.S. Mankin, *Sci. Adv.* **2018**, *4*, eaao3354.
3. R.K. Pachauri, L.A. Meyer, "Climate Change **2014**: Synthesis Report" *(IPCC, Geneva, Switzerland, 2014)*.
4. S. Xie, Q. Zhang, G. Liu, Y. Wang, *Chem. Commun.* **2016**, *52*, 35.
5. B. Kumar, M. Llorente, J. Froehlich, T. Dang, A. Sathrum, C. P. Kubiak, *Annu. Rev. Phys. Chem.* **2012**, *63*, 54.
6. S. M. Gupta, M. Tripathi, *Chinese Sci. Bull.* **2011**, *56*, 1639.
7. X. Chang, T. Wang, J. Gong, *Energy Environ. Sci.* **2016**, *9*, 2177.
8. E. D. Kosten, B. M. Kayes, H. A. Atwater, *Energy Environ. Sci.* **2014**, *7*, 1907.
9. Z. Yu, A. Raman, S. Fan, *Phys. Rev. Lett.* **2012**, *109*, 173901.
10. Y. Yao, J. Yao, V. K. Narasimhan, Z. Ruan, C. Xie, S. Fan, Y. Cui, *Nat. Commun.* **2012**, *3*, 664.
11. M.-L. Tsai, W.-C. Tu, L. Tang, T.-C. Wei, W.-R. Wei, S. P. Lau, L.-J. Chen, J.-H. He, *Nano. Lett.* **2016**, *16*, 309.
12 Y.-L. Tsai, K.-Y. Lai, M.-J. Lee, Y.-K. Liao, B. S. Ooi, H.-C. Kuo, J.-H. He, *Prog. Quantum Electron.* **2016**, *49*, 1.
13 C. Cho, S. Jeong, H.-J. Choi, N. Shin, B. Kim, E.-C. Jeon, J.-Y. Lee, *Adv. Opt. Mater.* **2015**, *3*, 1697.
14 W. Lee, S. Jeong, C. Lee, G. Han, C. Cho, J.-Y. Lee, B. J. Kim, *Adv. Energy Mater.* **2017**, *7*, 1602812.
15. Y. Wang, T. Li, Y. Yao, X. Li, X. Bai, C. Yin, N. Williams, S. Kang, L. Cui, L. Hu, *Adv. Energy Mater.* **2018**, *8*, 1703136.
16. X. Li, J. Yu, M. Jaroniec, Hierarchical photocatalysts, *Chem. Soc. Rev*. **2016**, *45*, 2603.
17. L. Chen, X. Tang, P. Xie, J. Xu, Z. Chen, Z. Cai, P. He, H. Zhou, D. Zhang, T. Fan, *Chem. Mater*. **2018**, *30*, 799.
18. F. Carn, A. Colin, M.-F. Achard, H. Deleuze, E. Sellier, M. Birot, R. Backov, *J. Mater. Chem.* **2004**, *14*, 1370.
19. N. Brun, S. Ungureanu, H. Deleuze, R. Backov, *Chem. Soc. Rev.* **2011**, *40*, 771.
20. M. S. Silverstein, *Polymer* **2017**, *126*, 261.
21. A. Roucher, M. Depardieu, D. Pekin, M. Morvan, R. Backov, *Chem. Rec.* **2018**, *18*, 776.
22. P. Gaikwad, S. Ungureanu, R. Backov, K. Vynck, R. A. L. Vallée, *Optic Express* **2014**, *22*, 7503.

23. N. Bachelard, P. Gaikwad, R. Backov, P. Sebbah, R. A. L. Vallée, *ACS Photonics* **2014**, *1*, 1206.

24. P. Gaikwad, N. Bachelar, P. Sebbah, R. Backov, R. A. L. Vallée, *Adv. Optical Mater.* **2015**, *3*, 1640.

25. E. A. Sosnov, A. A. Malkov, A. A. Malygin, *Russ. Chem. Rev.* **2010**, *79*, 907.

26. F. Carn, A. Colin, M.F. Achard, H. Deleuze, C. Sanchez, R. Backov, *Adv. Mat.* **2005,** *17*, 62.

27. F. Carn, M.-F. Achard, O. Babot, H. Deleuze, S. Reculusa, R. Backov, *J. Mat. Chem.* **2005**, *15*, 3887.

28. D. Vorkapic, T Matsoukas, *J. Am. Ceram. Soc.* **1998**, *81***,** 2815.

29. H. Zhang, J.F. Banfield, *J. Mater. Res.* **2000**, *15*, 437.

30. M. Thommes, K. Kaneko, A. V. Neimark, J. P. Olivier, F. Rodriguez-Reinoso, J. Rouquerol, K. S. W. Sing, "*Physisorption of gases, with special reference to the evaluation of surface area and pore size distribution*" (**2015** IUPAC Tech. Rep.,).

31. D. S. Wiersma, A. Muzzi, M. Colocci, and R. Righini, *Phys. Rev. E* **2000**, *62*, 6681.

32. J. X. Zhu, D. J. Pine, D. A. Weitz, *Phys. Rev. A* **1991**, *44*, 3948.

33. J.-M. Herrmann, *Top. Catal.* **2005**, *34*, 49.

34. E. Carbonell, F. Ramiro-Manzano, I. Rodriguez, A. Corma, F. Meseguer, H. Garcia, *Photochem. Photobiol. Sci.* **2008**, *7*, 931.

35 M. Destribats, B. Faure, M. Birot, O. Babot, V. Schmitt, R. Backov, *Adv. Funct. Mater.* **2012**, *22*, 2642.

SUPPLEMENTARY MATERIALS

Section 1: Photonic investigations

Section 2: Photocatalytic methodology

Section 3: Kinetic modelling

Figs. S1 to S11

Tables S1 to S9

Equations S1 to S43

TOC entry.

Novel TiO_2@Si(HIPE) Monolithic Macrocellular Foams offer the path for real 3D photo-driven CO_2 conversion at the millimeter thickness length scale, configuration where "thicker is better" appears as a new paradigm. The light trapping scenario and the associated photo-induced electron within the foams both limit back-reactions and promote outstanding selectivity toward methane, and even ethane generation through C-C coupling reaction.

Keywords: Porous materials; CO_2 photo-reduction, heterogeneous catalysis, sol-gel process, integrative chemistry.

Sophie Bernadet[1,2], Eugénie Tavernier[2], Duc-Minh Ta[1], Renaud A. L. Vallée[1], Serge Ravaine[1,*], Antoine Fécant[2,*] and Rénal Backov[1,3,*]

Bulk Photo-Driven CO_2 Conversion through TiO_2@Si(HIPE) Monolithic Macrocellular Foams